Analysis of instability patterns in non-Boussinesq mixed convection using a direct numerical evaluation of disturbance integrals

Sergey A. Suslov

Department of Mathematics and Computing and Computational Engineering and Science Research Centre, University of Southern Queensland, Toowoomba, Queensland 4350, Australia

Abstract

The Fourier integrals representing linearised disturbances arising from an initially localised source are evaluated numerically for natural and mixed convection flows between two differentially heated plates. The corresponding spatio-temporal instability patterns are obtained for strongly non-Boussinesq high-temperature convection of air and are contrasted to their Boussinesq counterparts. A drastic change in disturbance evolution scenarios is found when a large cross-channel temperature gradient leads to an essentially nonlinear variation of the fluid's transport properties and density. In particular, it is shown that non-Boussinesq natural convection flows are convectively unstable while forced convection flows can be absolutely unstable. These scenarios are opposite to the ones detected in classical Boussinesq convection. It is found that the competition between two physically distinct instability mechanisms which are due to the action of the shear and the buoyancy are responsible for such a drastic change in spatio-temporal characteristics of instabilities. The obtained numerical results confirm and complement semi-analytical conclusions of [1] on the absolute/convective instability transition in non-Boussinesq mixed convection. Generic features of the chosen numerical approach are discussed and its advantages and shortcomings are reported.

Key words:
PACS: 47.20Bp, 47.55.P, 47.15.Fe, 47.15.Rq, 47.20.Ft

1 Introduction

Convection between differentially heated vertical plates has been actively studied over several decades. After the analysis of such flows was pioneered in [2–4]

more than a half of a century ago, various aspects of this problem have since been addressed by many authors: experimentally in [5], numerically in [6] and [7], from a stability point of view in [8] and [9] just to name a few. More recently the current author conducted a comprehensive investigation of stability of such flows under the non-Boussinesq conditions [10–13]. In such regimes the temperature difference between the channel walls is so large that the fluid's transport property and density variations in the flow domain become strongly nonlinear and reach up to 30% of the average values [14]. This in turn leads to a qualitative change in flow characteristics such as, for example, the drift speed of convection rolls which was detected experimentally [15–17]. The corresponding analysis was enabled by employing the Low-Mach-number approximation of the compressible Navier-Stokes equations suggested in [18–20]. As a result a new physical parameter, the non-dimensional difference between the walls characterising the strength of non-Boussinesq effects is introduced along with the conventional Reynolds, Grashof and Prandtl numbers characterising the strength of the forced through-flow, the role of the buoyancy and the ratio of the thermal and viscous fluid properties, respectively.

In brief, the flows in the considered geometry exhibit the following features (the reader is referred to [11,12,21] for details). A steady basic flow exists away from the channel ends. It results from the competition between the buoyancy forces associated with nonlinear (non-Boussinesq) density variations and the imposed pressure gradient. The basic flow becomes linearly unstable with respect to two-dimensional shear-driven disturbances associated either with the inflection point of the basic velocity profile (at small Reynolds numbers) or with boundary layers (at larger Reynolds numbers) [11]. The pressure gradient defines the preferred drift direction of the disturbances. For large temperature differences between the walls the basic flow loses its symmetry and a new buoyancy-driven instability mode occurs near the cold wall. It has a preferred downward propagation direction. The interplay and interaction between these instability modes renders the problem interesting and challenging for the analysis.

The most recent semi-analytical study reported in [1] and concerned with the influence of non-Boussinesq effects on the physical mechanisms driving linear spatio-temporal instabilities of mixed convection revealed an enormous diversity of possible flow evolution scenarios: ten parametric regions have been identified for strongly non-Boussinesq regime alone, each corresponding to its own instability pattern. This wealth of flow behaviours is due to the existence of two physically distinct mechanisms of instabilities discovered earlier [10,11]: shear-driven and buoyancy-driven. Depending on the chosen values of the governing physical parameters each instability mode results in either convectively or absolutely unstable wave envelopes.

The conventional definitions of absolute and convective instabilities relate to

the dynamics of initially localised disturbances at a fixed spatial location (in a stationary frame). If the growing disturbances spread and eventually occupy the complete flow domain, then the instability is absolute. On the other hand, if growing disturbances propagate away leaving an undisturbed field behind, then the instability is convective. In other words, if in a stationary frame the edges of a disturbance envelope move in the same direction, then instability is convective, while if they propagate in the opposite directions the instability is absolute. Typical examples of a convectively and absolutely unstable systems are plane Poiseuille flow [22] and natural convection in a vertical fluid layer in the Boussinesq limit [13], respectively.

The investigation reported in [1] identified a complete range of theoretically possible instability scenarios. However some of the instability regions have been found to occupy very small areas of the parameter space. Therefore the question arises on the likelihood of detecting and distinguishing the corresponding instability structures in direct numerical simulations or experiments. Thus the goals of the present work are to compute the actual disturbance fields and to identify their characteristic features as relevant to DNS and experimental investigations. In pursuing these goals we will also identify the major differences between typical shear- and buoyancy-driven instability patterns and will contrast the patterns existing in the Boussinesq limit and in strongly non-Boussinesq conditions. It will be shown that the differences are drastic and the values of the governing parameters will be chosen for our computations to demonstrate them in the clearest way.

The above goals are fully achieved via the direct numerical evaluation of the Fourier integrals describing evolution of disturbances. This approach is chosen because it is less computationally demanding than direct numerical simulations of a full set of the governing equations. Its other important advantage is that it enables a straightforward separation of competing instabilities so that their individual features can be analysed. However since only linearised equations are integrated, the method has its obvious limitations: it cannot predict the saturation of the computed instability patterns or nonlinear interactions between instability modes. Thus only initial stages of instability development are simulated. In section 3.1 we also discuss a number of general issues associated with the unavoidable truncation of the integration interval which have to be dealt with carefully. Subsequently, we report on specific computational measures which have been implemented to guarantee the correct interpretation of the spatio-temporal characteristics of computed disturbance fields.

The overall structure of this paper is as follows. Section 2 formulates the physical problem and introduces a set of non-dimensionalised linearised Low-Mach Number equations. This is followed by the derivation of the Fourier integrals describing the evolution of disturbances superposed onto the parallel

basic flow. Section 3 proceeds with a discussion of the numerical procedure and subsequently presents and discusses the results for two thermal regimes: the classical Boussinesq limit of small temperature differences and the strongly non-Boussinesq regime corresponding to the temperature difference of $360K$ between the channel walls. Section 4 summarises the reported findings.

2 Problem definition and linearised equations

We consider a mixed convection flow in a tall vertical channel of the width H and height $L \gg H$ with isothermal vertical walls maintained at the different temperatures T_h^* and T_c^* (asterisks denote dimensional quantities). A uniform downward gravitational field g is parallel to the walls. In the case of finite temperature differences $\Delta T = T_h^* - T_c^* \gg 0$ the flow is described by the low-Mach-number momentum and thermal energy equations [20,18] complimented by the ideal gas equation of state relating the fluid density ρ^* and the temperature T^* and the constitutive equations for the specific heat at constant pressure c_p^*, the dynamic viscosity μ^* and the thermal conductivity k^*. The properly non-dimensionalised form of these equations is discussed in [1] and references therein and will not be repeated here for brevity.

As discussed in [1] the problem is characterised by the Prandtl number $Pr \equiv \mu_r c_{pr}/k_r = 0.71$ (for air), the non-dimensional temperature difference between the walls $\epsilon \equiv \Delta T/(2T_r)$, the Grashof number $Gr \equiv 2\rho_r^2 g\epsilon H^3/\mu_r^2$, and the the Reynolds number $Re = \rho_r U_r H/\mu_r$. These parameters are defined using the reference temperature $T_r \equiv \left(T_h^* + T_c^*\right)/2$ and the characteristic longitudinal speed

$$U_r = -H^2 \left(\Pi_{\text{top}}^* - \Pi_{\text{bottom}}^*\right)/(12\mu_r L)\,,$$

where Π^* is the dynamic pressure in the channel. The subscript r signifies that all physical fluid properties used to define the above governing parameters correspond to air at the reference temperature of $T_r = 300K$. Two thermal regimes of $\epsilon = 0.005$ (Boussinesq limit) and $\epsilon = 0.6$ (strongly non-Boussinesq regime) which correspond to the dimensional temperature difference between the walls of 3 and $360K$ will be considered.

As discussed in [11] the steady parallel basic flow with velocity components $u_0 = 0$, $v_0 = v_0(x)$, temperature profile $T_0 = T_0(x)$, and constant pressure gradient $\mathrm{d}\Pi_0/\mathrm{d}y = \text{const.}$ in the longitudinal y-direction can exist in a channel sufficiently far away from the ends. Figure 1 shows typical mixed convection basic flow parallel velocity and temperature profiles. This flow becomes unstable with respect to two-dimensional disturbances $u' = u'(x, y, t)$, $v' = v'(x, y, t)$, $T' = T'(x, y, t)$, $\Pi' = \Pi'(x, y, t)$. The disturbances satisfy the homogeneous boundary conditions $u' = v' = T' = 0$ at the left and right walls

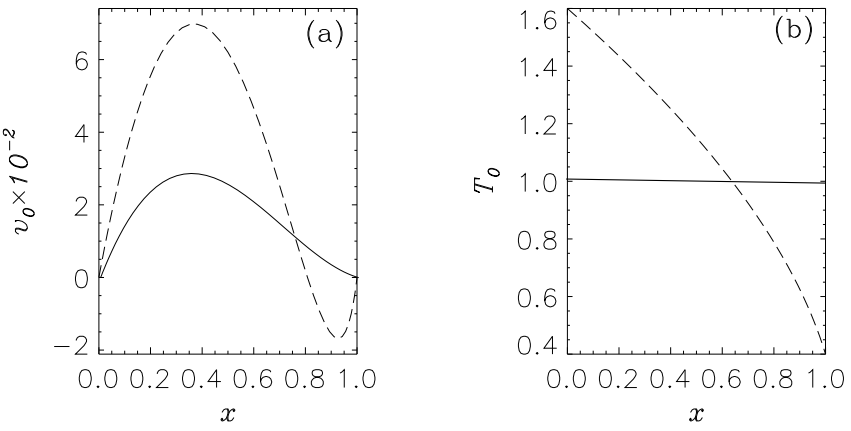

Fig. 1. Typical mixed convection velocity (a) and temperature (b) basic flow profiles: solid and dashed lines correspond to strongly and weakly forced convection at $(Re, Gr, \epsilon) = (2000, 13000, 0.005)$ and $(Re, Gr, \epsilon) = (260, 46000, 0.6)$, respectively.

located at $x = 0$ and $x = 1$, respectively. Upon linearisation about the basic flow (which is found numerically using the integral Chebyshev collocation method of [23] as discussed in [11]), the non-dimensional momentum, thermal energy and continuity equations governing infinitesimal disturbances become

$$\rho_0 \left(\frac{\partial u'}{\partial t} + v_0 \frac{\partial u'}{\partial y} \right) + \frac{\partial \Pi'}{\partial x} - \frac{2}{3} \frac{\partial}{\partial x} \left[\mu_0 \left(2 \frac{\partial u'}{\partial x} - \frac{\partial v'}{\partial y} \right) \right] - \mu_0 \left(\frac{\partial^2 u'}{\partial y^2} + \frac{\partial^2 v'}{\partial x \partial y} \right) - \frac{\partial \mu'}{\partial y} D v_0 = F_u \,, \tag{1}$$

$$\rho_0 \left(\frac{\partial v'}{\partial t} + u' D v_0 + v_0 \frac{\partial v'}{\partial y} \right) + \frac{\partial \Pi'}{\partial y} + \frac{Gr}{2\epsilon} \rho' - \frac{2}{3} \mu_0 \left(2 \frac{\partial^2 v'}{\partial y^2} - \frac{\partial^2 u'}{\partial x \partial y} \right) - \frac{\partial}{\partial x} \left[\mu_0 \left(\frac{\partial v'}{\partial x} + \frac{\partial u'}{\partial y} \right) + \mu' D v_0 \right] = F_v \,, \tag{2}$$

$$\rho_0 \left(\frac{\partial T'}{\partial t} + u' D T_0 + v_0 \frac{\partial T'}{\partial y} \right) - \frac{1}{Pr} \left[\frac{\partial}{\partial x} \left(k' D T_0 + k_0 \frac{\partial T'}{\partial x} \right) + k_0 \frac{\partial^2 T'}{\partial y^2} \right] = F_T \,, \tag{3}$$

$$\frac{\partial \rho'}{\partial t} + u' D \rho_0 + v_0 \frac{\partial \rho'}{\partial y} + \rho_0 \left(\frac{\partial u'}{\partial x} + \frac{\partial v'}{\partial y} \right) = F_c \,, \tag{4}$$

where $D \equiv \frac{\mathrm{d}}{\mathrm{d}x}$, $F_{u,v,T,c}$ are forcing terms and non-dimensional quantities ρ_0, μ_0 and k_0 are given in terms of the non-dimensional basic flow temperature $T_0(x)$ as

$$\rho_0 = \frac{1}{T_0} \,, \quad \mu_0 = T_0^{3/2} \left(\frac{1 + S_\mu}{T_0 + S_\mu} \right) \,, \quad k_0 = T_0^{3/2} \left(\frac{1 + S_k}{T_0 + S_k} \right) \,.$$

According to [24], the non-dimensional Sutherland constants for air are $S_\mu = S_\mu^*/T_r = 0.368$ and $S_k = S_k^*/T_r = 0.648$ for $T_r = 300K$. Note that even

though the Reynolds number does not appear in system (1)–(4) explicitly it is an important problem parameter which implicitly defines the magnitude of the basic flow velocity v_0. Disturbances of fluid properties are then given by

$$\rho' = \frac{\mathrm{d}\rho_0}{\mathrm{d}T_0}T' = -\frac{T'}{T_0^2}\,, \tag{5}$$

$$\mu' = \frac{\mathrm{d}\mu_0}{\mathrm{d}T_0}T' = \frac{1+S_\mu}{2}\frac{T_0+3S_\mu}{(T_0+S_\mu)^2}\sqrt{T_0}T'\,, \tag{6}$$

$$k' = \frac{\mathrm{d}k_0}{\mathrm{d}T_0}T' = \frac{1+S_k}{2}\frac{T_0+3S_k}{(T_0+S_k)^2}\sqrt{T_0}T'\,. \tag{7}$$

Introduce the Fourier transform in y and the Laplace transform in t of the disturbance quantities and the corresponding inverse transforms so that

$$\tilde{f}(\alpha,x,t) = \int_{-\infty}^{\infty} f'(x,y,t)\mathrm{e}^{-\mathrm{i}\alpha y}\,\mathrm{d}y\,, \quad f'(x,y,t) = \frac{1}{2\pi}\int_{-\infty}^{\infty}\tilde{f}(\alpha,x,t)\mathrm{e}^{\mathrm{i}\alpha y}\,\mathrm{d}\alpha\,,$$

$$\hat{\tilde{f}}(\alpha,\sigma,x) = \int_{-\infty}^{\infty}\tilde{f}(\alpha,x,t)\mathrm{e}^{-\sigma t}\,\mathrm{d}t\,, \quad \tilde{f}(\alpha,x,t) = \frac{1}{2\pi\mathrm{i}}\int_{L-\mathrm{i}\infty}^{L+\mathrm{i}\infty}\hat{\tilde{f}}(\alpha,\sigma,x)\,\mathrm{e}^{\sigma t}\,\mathrm{d}\sigma\,.$$

Then the forced system corresponding to (1)–(7) becomes

$$\begin{aligned}\rho_0(\sigma+\mathrm{i}\alpha v_0)\hat{\tilde{u}} + D\hat{\tilde{\Pi}} - \frac{2}{3}D\left[\mu_0\left(2D\hat{\tilde{u}} - \mathrm{i}\alpha\hat{\tilde{v}}\right)\right] \\ + \alpha\left[\mu_0\left(\alpha\hat{\tilde{u}} - \mathrm{i}D\hat{\tilde{v}}\right) - \mathrm{i}\frac{\mathrm{d}\mu_0}{\mathrm{d}T_0}\hat{\tilde{T}}Dv_0\right] = \hat{\tilde{F}}_u\,,\end{aligned} \tag{8}$$

$$\begin{aligned}\rho_0\left(\sigma\hat{\tilde{v}} + \hat{\tilde{u}}Dv_0 + \mathrm{i}\alpha v_0\hat{\tilde{v}}\right) + \mathrm{i}\alpha\hat{\tilde{\Pi}} - \frac{Gr}{2\epsilon}\frac{\hat{\tilde{T}}}{T_0^2} - D\left[\mu_0\left(D\hat{\tilde{v}} + \mathrm{i}\alpha\hat{\tilde{u}}\right) + \frac{\mathrm{d}\mu_0}{\mathrm{d}T_0}Dv_0\hat{\tilde{T}}\right] \\ + \frac{2}{3}\alpha\mu_0\left[2\alpha\hat{\tilde{v}} + \mathrm{i}D\hat{\tilde{u}}\right] = \hat{\tilde{F}}_v\,,\end{aligned} \tag{9}$$

$$\rho_0\left(\sigma\hat{\tilde{T}} + \hat{\tilde{u}}DT_0 + \mathrm{i}\alpha v_0\hat{\tilde{T}}\right) - \frac{1}{Pr}\left[D^2\left(k_0\hat{\tilde{T}}\right) - \alpha^2 k_0\hat{\tilde{T}}\right] = \hat{\tilde{F}}_T\,, \tag{10}$$

$$\rho_0\left(\sigma\hat{\tilde{T}} + \hat{\tilde{u}}DT_0 + \mathrm{i}\alpha v_0\hat{\tilde{T}}\right) - D\hat{\tilde{u}} - \mathrm{i}\alpha\hat{\tilde{v}} = \hat{\tilde{F}}_c\,, \tag{11}$$

where the right-hand sides are the Fourier-Laplace transforms of the forcing terms. In this work we focus on determining asymptotic spatio-temporal dynamics caused by initially localised disturbances. Thus it is convenient to consider impulse excitation of the form

$$\begin{aligned}F_u = a_u(x)\delta(y)\delta(t)\,, \quad F_v = a_v(x)\delta(y)\delta(t)\,, \\ F_T = a_T(x)\delta(y)\delta(t)\,, \quad F_c = a_c(x)\delta(y)\delta(t)\,,\end{aligned} \tag{12}$$

where δ denotes the Dirac delta function and $a_{u,v,T,c}(x)$ are unspecified at this

stage functions. Then

$$\hat{\tilde{\mathbf{F}}} = \left(\hat{\tilde{F}}_u, \hat{\tilde{F}}_v, \hat{\tilde{F}}_T, \hat{\tilde{F}}_c\right)^T = (a_u(x), a_v(x), a_T, a_c(x))^T \,. \tag{13}$$

System (8)–(11) is solved numerically using the integro-differential Chebyshev collocation method of [25,23] as described in [11]. After discretisation the problem reduces to a linear algebraic system written in a matrix form as

$$\mathbf{L}_{\alpha,\sigma}\mathbf{w} \equiv (\mathbf{A}(\alpha) - \sigma\mathbf{B})\mathbf{w} = \mathbf{f} \,, \tag{14}$$

where $\mathbf{w}$ is a discretised version of a vector of unknowns $\left(D^2\hat{\tilde{u}}, D^2\hat{\tilde{v}}, D^2\hat{\tilde{T}}, \hat{\tilde{\Pi}}\right)^T$, see [11], and $\mathbf{f}$ is the discretised version of $\hat{\tilde{\mathbf{F}}}$. Once the second derivatives of the disturbances are found the actual flow fields are obtained at the collocation points $x_n = \cos[\pi(n-1)/(N-1)]$, $n = 1, 2, \ldots, N$, where N is the total number of the collocation points, by multiplying the vectors of second derivatives by a standard integration matrix [23]. This procedure enables a higher accuracy of the results with negligible additional computational cost. For further convenience we implicitly choose functions $a_{u,v,T,c}(x)$ in such a way that their discretised versions are non-zero only at a single collocation point (discrete version of the Dirac delta function in x) so that the discrete forcing term becomes

$$\mathbf{f} = (\underbrace{0, \ldots, \overbrace{b_u}^{n_u}, \ldots, 0}_{N}, \underbrace{0, \ldots, \overbrace{b_v}^{n_v}, \ldots, 0}_{N}, \underbrace{0, \ldots, \overbrace{b_T}^{n_T}, \ldots, 0}_{N}, \underbrace{0, \ldots, \overbrace{b_c}^{n_c}, \ldots, 0}_{N})^T \,. \tag{15}$$

Constants $b_{u,v,T,c}$ are equal to 0 or 1 and may be chosen independently so that the influence of the disturbances on the individual momentum, thermal energy or continuity equations may be studied. Values of $n_{u,v,T,c}$ ($2 \le n_{u,v,T,c} \le N-1$) define the collocation point at which the disturbances are introduced and may be chosen independently as well. Although the asymptotic solution does not depend on this choice (assuming that the eigenfunctions of the linearised problem (16), see below) do not have any singularities within the computational domain) it might be of interest to look at the initial stages of the disturbance development (receptivity) when the solution does depend on the values of $n_{u,v,T,c}$.

If $\mathbf{f} = \mathbf{0}$ then (14) reduces to an algebraic generalised eigenvalue problem

$$\mathbf{L}_{\alpha,\sigma}\mathbf{w} = \mathbf{0} \tag{16}$$

which defines the dispersion relation $\sigma_j = \sigma_j(\alpha)$, where the complex eigenvalues $\sigma_j = \sigma_j^R + \mathrm{i}\sigma_j^I$, $j = 1, 2, \ldots$ are the complex temporal amplification rates of the corresponding disturbance eigenmodes $\mathbf{w}_j$ whose longitudinal structure

is given by wavenumber α. We also define the corresponding adjoint problem and adjoint eigenfunctions by

$$\mathbf{L}^{\dagger}_{\alpha,\sigma}\mathbf{w}^{\dagger} \equiv (\mathbf{A}^{*T}(\alpha) - \sigma^{*}\mathbf{B}^{*T})\mathbf{w}^{\dagger} = \mathbf{0}\,, \tag{17}$$

and normalise them so that $\langle \mathbf{w}^{\dagger}_i, \mathbf{B}\mathbf{w}_j \rangle = \delta_{ij}$, where the angle brackets denote a standard inner product for discrete complex $4N$-component vectors $\mathbf{a}$ and $\mathbf{b}$: $\langle \mathbf{a}, \mathbf{b} \rangle = \sum_{k=1}^{4N} a^{*}_k b_k$ and stars denote complex conjugate.

It is usually suggested (see, for example, [26]) to look for the solution of (14) via the eigenfunction expansion. Strictly speaking this is not rigorously justified. Indeed, operator $\mathbf{L}_{\alpha,\sigma}$ is not self-adjoint, its eigenfunctions are not orthogonal and the completeness of eigenfunctions is hard, if possible at all, to establish. So instead we look for a projection of solution of (14) onto a space spanned by M distinct eigenfunctions of the corresponding eigenvalue problem

$$\hat{\tilde{\mathbf{w}}}_p(\alpha, \sigma, x_n) = \sum_{j=1}^{M} A_j(\alpha, \sigma)\mathbf{w}_j(\alpha, \sigma, x_n)\,. \tag{18}$$

Projection coefficients A_j are determined from the inner product of (14) with $\mathbf{w}^{\dagger}_j$ using the orthogonality of adjoint and direct eigenfunctions:

$$A_j(\alpha, \sigma) = \frac{\left\langle \mathbf{w}^{\dagger}_j(\alpha), \mathbf{f} \right\rangle}{\sigma_j - \sigma}\,. \tag{19}$$

The projection of a solution in a physical space is obtained by applying the inverse Laplace and Fourier transforms to (18) which leads to expression (20) below. The theoretical details are quite involved and the interested reader is refereed to [1] for a comprehensive discussion. Here we just mention in passing that since the algebraic eigenvalue problem (16) has a finite number of eigenvalues σ_j, the inverse Laplace transform integration contour can be chosen as a vertical line $\sigma^R = L$ in the complex σ-plane to the right of all eigenvalues σ_j, i.e. $L > \max_j \sigma^R_j(\alpha)$. The contour is closed by an infinite semi-circle from the right for $t < 0$. Since in this case (18) does not have any singularities within the closed contour the inverse Laplace transform results in zero solution as required by the causality condition (no disturbances for $t < 0$). For $t > 0$ the contour is closed by an infinite semi-circle from the left of L. Now the contour encloses the finite number of pole singularities associated with eigenvalues σ_j. Application of the residue theorem then leads to

$$\tilde{\mathbf{w}}_p(\alpha, x_n, t) = \sum_{j=1}^{M} \left\langle \mathbf{w}^{\dagger}_j(\alpha), \mathbf{f} \right\rangle \mathbf{w}_j(\alpha, x_n) \mathrm{e}^{\sigma_j t}\,.$$

The projected solution in a physical space then is given by the inverse Fourier

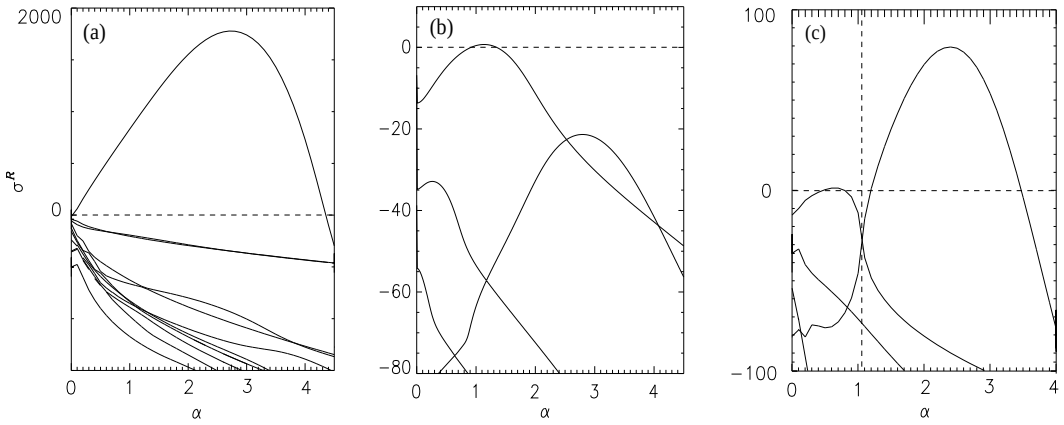

Fig. 2. Instability amplification rates σ_j^R for various modes in (a) mixed convection at $(Re, Gr, \epsilon) = (2000, 13000, 0.005)$, (b) natural convection at $(Re, Gr, \epsilon) = (0, 10000, 0.6)$ and (c) mixed convection at $(Re, Gr, \epsilon) = (260, 46000, 0.6)$. In plot (c) the buoyancy- and shear-driven instabilities are found for wavenumbers to the left and to the right of the vertical dotted line, respectively.

transform

$$\mathbf{w}_p(x_n, y, t) = \frac{1}{2\pi} \sum_{j=1}^{M} \int_{-\infty}^{\infty} \left\langle \mathbf{w}_j^\dagger(\alpha), \mathbf{f} \right\rangle \mathbf{w}_j(\alpha, x_n) \mathrm{e}^{\sigma_j(\alpha)t + \mathrm{i}\alpha y} \, \mathrm{d}\alpha \,. \tag{20}$$

As discussed in [1] the integrand in (20) evaluated at $-\alpha$ is a complex conjugate of that evaluated at α. Thus we use the following equivalent form of (20) to reduce the cost of numerical integration:

$$\mathbf{w}_p(x_n, y, t) = \frac{1}{\pi} \mathrm{Re} \left\{ \sum_{j=1}^{M} \int_{0}^{\infty} \left\langle \mathbf{w}_j^\dagger(\alpha), \mathbf{f} \right\rangle \mathbf{w}_j(\alpha, x_n) \mathrm{e}^{\sigma_j(\alpha)t + \mathrm{i}\alpha y} \, \mathrm{d}\alpha \right\} \tag{21}$$

Since the asymptotic behaviour of $\mathbf{w}_p(x_n, y, t)$ as $t \to \infty$ is determined by the modes with the largest amplification rates σ_j^R, it is sufficient to perform integration only for M linearly unstable modes for which $\sigma_j^R(\alpha) > 0$ for some range of wavenumbers α if only a long-term solution is of interest (for this purpose choosing $M = 2$ suffices in the current physical problem). However, this low order truncation is inaccurate for small time when contributions to the projected solution from the unaccounted decaying modes are not negligible. Implications of this aspect will be discussed below.

3 Numerical evaluation of the Fourier integrals

3.1 General issues

Direct evaluation of the inverse Fourier transform integral (21) has been performed at selected points in the parameter space to confirm the analytical results obtained in [1] and to achieve further insight into the physics of non-Boussinesq mixed convection instabilities as contrasted to their counterparts in the Boussinesq limit. The integration has been performed over the interval of wavenumbers $0 \leq \alpha \leq 4$ which in all cases contained all modes with $\sigma_j^R(\alpha) \geq 0$, see Figure 2. The NAG library subroutine D01GAF was used with the wavenumber step $\Delta\alpha = 0.01$. This choice guarantees unaliased solution [27] which is accurate for considered time intervals (discussion of the influence of the integration step size on the accuracy of the results is given, for example, by [26]). All computations were performed with $M = 3$, see equation (18). This ensures slightly better accuracy for small times than in a traditional approach when only one linearly unstable mode is considered (see, for example, [22]). In addition, this enables capturing both growing shear and buoyancy modes and at least one decaying mode, see figure 2. Unless stated otherwise in the text the initial disturbance pulses were chosen to be in the middle of the channel at $x_{n_u} = x_{n_v} = x_{n_T} = x_{n_c} = 0.5$ and $y = 0$. The forcing contributions to all governing equations were equal $b_u = b_v = b_T = b_c = 1$ (see equation (15)).

We note however that although the major goal of this numerical investigation is to trace the spatio-temporal evolution of initially localised (ideally, pulse-like) flow disturbances, the finite truncations of the Fourier wavenumber interval in the longitudinal direction and of the eigenfunction expansion series (18) make it practically impossible to consider initial conditions with strictly finite support. Inevitably the numerical initial condition is given as a combination of a localised structure whose evolution is of major interest and the low-level background noise distributed throughout the computational domain. In both convectively and absolutely unstable regimes this spatially distributed noise is amplified and tends to obscure the spatio-temporal dynamics of the localised structure of interest. Thus its dynamics can only be resolved for a limited time while the structure-to-noise ratio within the observed domain remains sufficiently large. An attempt to perform time integration after the initially localised structure dominating the noise has propagated away (in convectively unstable regimes) or after the initial noise is sufficiently amplified throughout the computational domain (in absolutely unstable regimes) leads to the appearance of an extended spatially periodic pattern with a wavenumber approaching that of the most amplified wave and with an exponentially growing amplitude. It has nothing to do with the dynamics of a localised structure of interest. Therefore care should be taken when interpreting numerical integra-

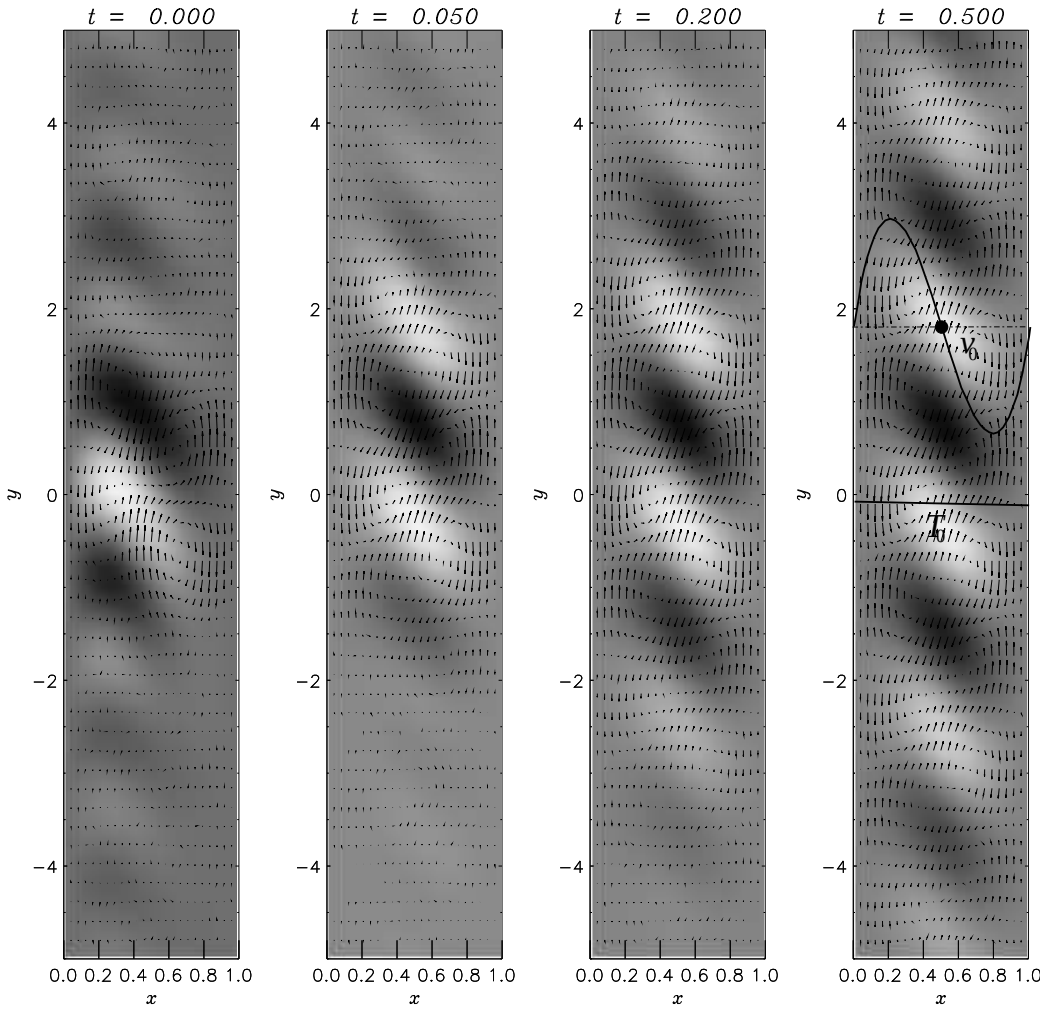

Fig. 3. Snapshots of the disturbance velocity (arrows) and temperature (shade plot) fields for $(Re, Gr, \epsilon) = (0, 8100, 0.005)$. Light areas correspond to the higher temperature. Solid circle shows the location of the inflection point of the basic flow velocity profile. Absolute instability.

tion results as will be shown in section 3.3.

3.2 Boussinesq convection at $\epsilon = 0.005$

To demonstrate the adequate resolution of the employed integration technique we first consider disturbance dynamics in two classical flow situations, namely, low-temperature natural and mixed convection flows whose spatio-temporal instability character has been investigated elsewhere [13,22].

Figure 3 shows the development of instability in a Boussinesq natural convection flow in a vertical channel with differentially heated walls. The basic flow

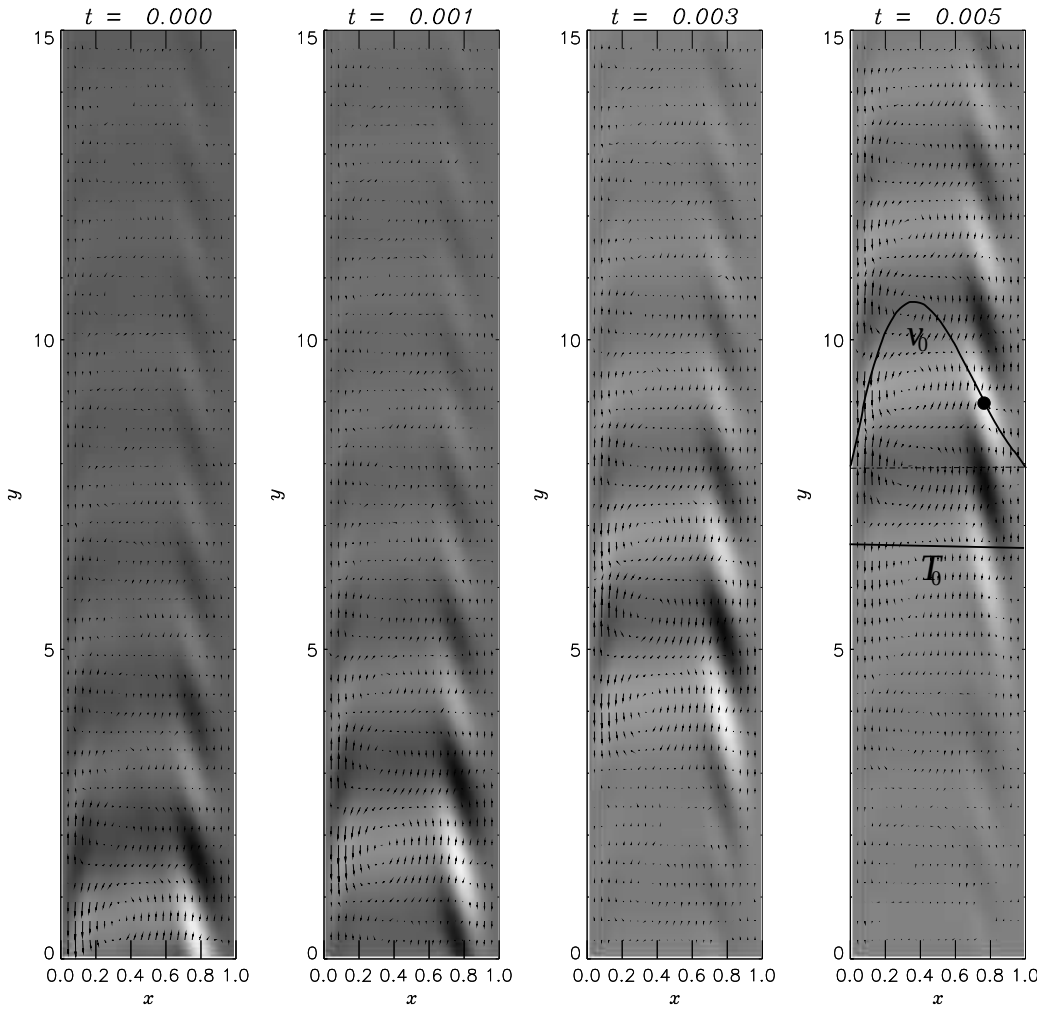

Fig. 4. Same as Fig. 3 but for $(Re, Gr, \epsilon) = (2000, 130000, 0.005)$. Convective instability.

velocity profile in this case is centro-symmetric with fluid rising along the left hot wall and descending along the right cold wall as sketched in the rightmost plot in figure 3. The asymptotic instability takes the form of counter-rotating cells centred along the mid-plane of the channel. Even if the initial disturbance is introduced at $(x, y) = (0.1, 0)$ (see the leftmost plot) its maximum shifts quickly to the centre of the channel where the inflection point of the cubic basic flow velocity profile is located. This confirms the classical inviscid (shear) [28] nature of instability in Boussinesq natural convection. As time progresses the magnitude of disturbances grows and the edges of the disturbance envelope propagate in the opposite directions. Therefore the instability is absolute.

The situation is qualitatively different in mixed convection flow at higher values of the Reynolds number and relatively small values of the Grashof num-

ber as seen from figure 4. In this case the basic flow velocity profile is of the Poiseuille type, i.e. close to parabolic with unidirectional upward flow, see the solid line in figure 1(a). The deviation from a parabolic shape is due to the buoyancy forces which encourage upward motion near the hot wall and suppress it near the cold one. As a result the basic velocity profile in figure 4 still has an inflection point which however moves closer to the cold wall. As seen from the rightmost plot in figure 4 the location of the disturbance maximum coincides with that of the inflection point of the basic velocity profile. However a somewhat weaker disturbance pattern now is seen near the cold wall as well. In contrast to the inflection point instability observed closer to the cold wall, the instability that arises near the hot wall is of a boundary-layer (Tollmien-Schlichting) type. When the ratio Re/Gr increases the inflection point of the basic velocity profile disappears and Tollmien-Schlichting instability becomes dominant. Regardless of whether the instability arises in the boundary layer or near the inflection point, the unidirectional upward primary flow is sufficiently strong so that it carries the growing localised disturbances away leaving an undisturbed field at any fixed spatial location. This is an example of a convective instability.

Note that as discussed in section 3.1 the low-dimensional projection of the pulse-like initial condition leads to a situation when the initial fields shown in the leftmost plots in figures 3 and 4 for $t = 0$ do not appear as highly localised structures. This is a direct consequence of the fact that only $M = 3$ eigenfunctions are used here to represent the complete solution. The fact that the Fourier integral (21) over a semi-infinite interval is approximated by an integral over a finite range $0 \leq \alpha \leq 4$ also contributes to the appearance of a small amplitude y-periodic component in the projected initial condition. These are the fundamental difficulties in simulating spatially localised structures using their Fourier decomposition. Increasing the number of modes M and the integration α interval can reduce such a spatial spread of an initial field but cannot remove it completely. Thus one has to be very careful in interpreting the numerical results which are supposed to distinguish between spatially extended and localised dynamics. Only when the neglected modes decay sufficiently quickly in comparison with the ones which are used in integration can one hope to obtain a direct visual confirmation of absolute or convective nature of a long-term instability by inspecting a series of field snap-shots such as the ones shown in figures 3 and 4. The difficulties with representing localised structures do not obscure the spatio-temporal nature of the developing instabilities in the two limiting cases considered above, but a more delicate procedure will be required to distinguish between the types of instabilities in non-Boussinesq mixed convection regimes discussed next.

3.3 Strongly non-Boussinesq convection at $\epsilon = 0.6$

As discussed in [10,11,1] at this large value of the non-dimensional temperature difference between the walls a physically different instability mode is present. It is not found in low temperature regimes (see figure 2(a)) and is an essentially non-Boussinesq effect. It has been shown in [10,11] that it is this new mode which destabilises the basic natural and near-natural convection flow at large values of ϵ. This occurs for significantly smaller values of the Grashof number than those at which the shear-driven instability settles in. The typical disturbance field arising in natural convection flows at large values of ϵ is depicted in figure 5. The following drastic differences are evident from comparison of figures 3 and 5. The instability arising in strongly non-Boussinesq natural convection has a much larger wavelength. The non-Boussinesq disturbance pattern is shifted toward the cold wall so that its maximum is located between the inflection point of the basic flow velocity profile and the right channel boundary, see the third plot in figure 5. Therefore this type of instability is not brought about by the classical shear-driven (inflection point) mechanism. As was argued by the author in [12,21] the physical reason for this instability is a highly nonlinear dependence of fluid density on the temperature: as seen in figure 5, the disturbance maximum is located in the region where the basic flow temperature gradient is steepest. The strong thermal non-uniformity of fluid near the cold wall creates favourable conditions for the formation of thermal disturbances. In addition, since the thermal conductivity and the viscosity of air decrease with temperature the dissipation effects are suppressed near the cold wall and the formed disturbance structures are more likely to survive. In turn these disturbances lead to the formation of denser lumps of overcooled fluid which subsequently drift down due to their negative buoyancy. Therefore we refer to this type of instability as buoyancy-driven. In contrast to natural convection in the Boussinesq limit the non-Boussinesq buoyancy disturbances have a preferred propagation direction. A major new feature of the non-Boussinesq instability demonstrated in figure 5 is that the propagation speed of buoyancy-driven disturbances is sufficiently large so that the initially localised disturbances move down faster than they extend. Thus a continuous source of perturbations is required in order to maintain this instability. This is the signature of convective instability which sets in non-Boussinesq natural convection in contrast to an absolute instability detected in the low-temperature regimes.

In mixed non-Boussinesq convection at moderate Reynolds numbers the buoyancy and shear-driven instabilities are found to co-exist [1]. The typical disturbance amplification rate diagram is shown in figure 2(c) which now has two positive maxima with substantially different magnitudes. To increase numerical accuracy and analyse the dynamics of two modes individually we split integral (21) into the sum of two partial integrals. These are taken over the

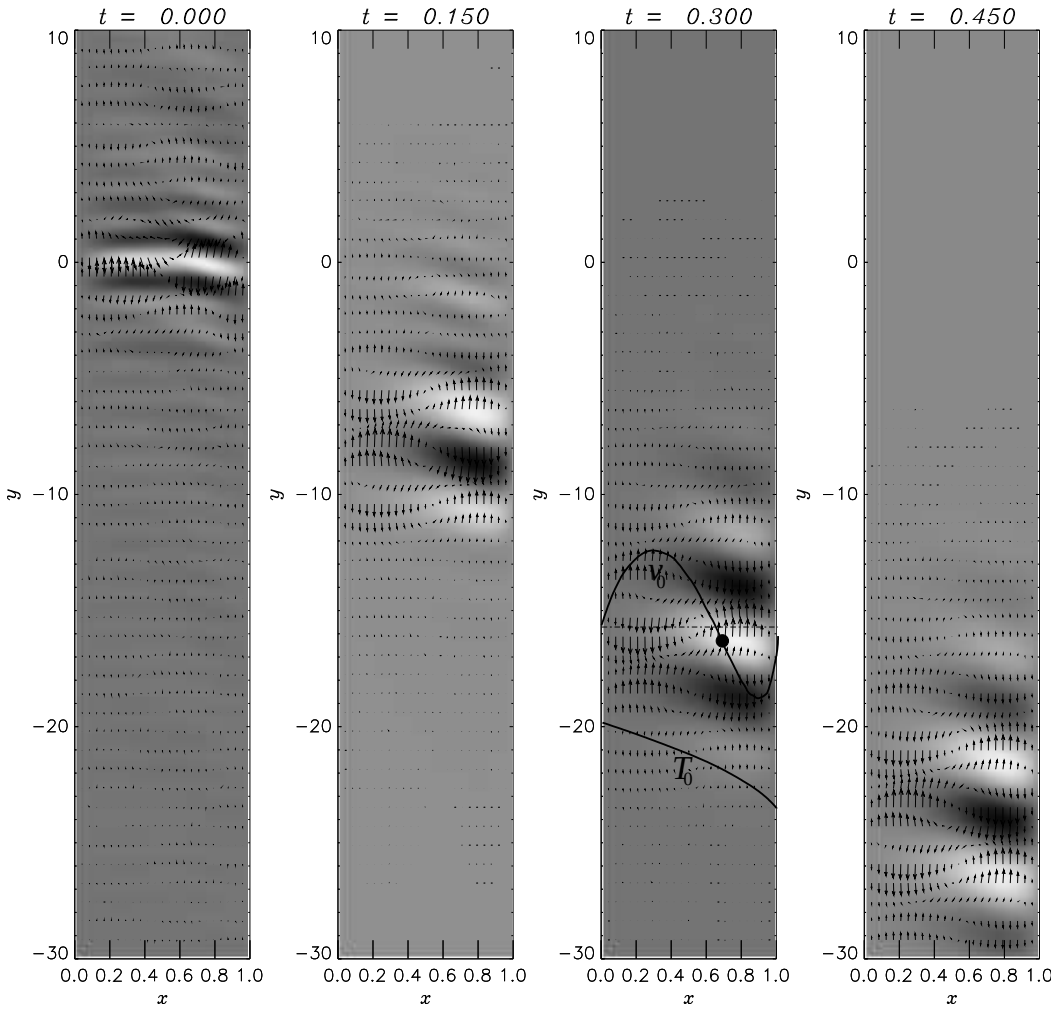

Fig. 5. Same as Fig. 3 but for $(Re, Gr, \epsilon) = (0, 10000, 0.6)$. Convective instability.

adjacent wavenumber ranges separated by the wavenumber at which the two top $\sigma^R(\alpha)$ curves forming the left and right maxima intersect in figure 2(c). This wavenumber value corresponds to the vertical dashed line. The two integrals then represent asymptotic contributions of different instability modes into the overall pattern. Note that it is possible that, instead of two intersecting $\sigma^R(\alpha)$ curves containing one positive maximum each, the two leading eigenvalues of a linearised problem (16) form two continuous non-intersecting lines. In this case the upper $\sigma^R(\alpha)$ curve would contain both positive maxima separated by a negative minimum and would be of interest. As noted in [1] the difference between the shear and buoyancy modes in such situations is somewhat blurred, yet we continue to distinguish between them by taking the "buoyancy mode" integral over the range from $\alpha = 0$ up to the minimum point of the top $\sigma^R(\alpha)$ curve and the "shear mode" integral over the interval to the right of this point. This is justified because for all values of the governing parameters the value of α at which the so-defined wave envelopes are

separated corresponds to $\sigma^R < 0$. Therefore asymptotically one will observe two well separated disturbance structures with different characteristic wavelengths propagating with different speeds. Each of these structures will be fully described by their own part of the overall Fourier integral (21). Figures 6–9 correspond to such individually computed wave envelopes.

The shear instability envelope in the strongly non-Boussinesq regimes depicted in figure 6 is very similar to those that exist in Boussinesq regimes. The localised disturbance initially introduced near the centre plane of the channel (see the leftmost plot) moves quickly toward the cold wall where the inflection point of the basic flow velocity profile shifts, see the rightmost plot. Then it forms a well defined wave envelope which propagates in the dominant direction of the primary flow (upwards in figure 6) determined by the direction of the applied pressure gradient. Note that the ripples seen in the two left plots in figure 6 are due to the truncation of the integration interval discussed above. These ripples disappear with time because the neglected part of the wave envelope which causes them initially has a negative amplification rate.

The series of computed snapshots presented in figure 6 illustrate the most typical features of shear-driven instability: its spatial patterns are most prominent in the vicinity of the inflection point of the basic flow velocity profile and they propagate in the direction of the primary flow. However in contrast to flow fields depicted in figures 3–5 it is difficult to establish the spatio-temporal character of the instability presented in figure 6. A superficial inspection of this figure might suggest that disturbances propagate away from their initial location so that the instability appears to be convective. Yet a thorough theoretical investigation conducted by the author in [1] showed that a set of parameters $(Re, Gr, \epsilon) = (260, 46000, 0.6)$ for which the flow fields are shown in figure 6 actually corresponds to the absolute instability regime (see stability diagrams in figures 13(a) and 14(a) in [1]). In order to resolve this apparent contradiction we proceed to examine the computed fields for the disturbance temperature T' and the disturbance kinetic energy

$$E'_k = \frac{u'^2 + v'^2}{2T_0} - \frac{v_0^2 T'}{2T_0^2}$$

near $y = 0$ where the disturbances are originally introduced. We define the corresponding time-dependent disturbance norms as

$$T_m = \max_{\substack{0 \le x \le 1 \\ y = 0}} (T') - \min_{\substack{0 \le x \le 1 \\ y = 0}} (T') \quad \text{and} \quad E_m = \max_{\substack{0 \le x \le 1 \\ y = 0}} (E'_k) - \min_{\substack{0 \le x \le 1 \\ y = 0}} (E'_k) \ . \quad (22)$$

The difference between the global maximum and minimum values of the disturbance quantities along the crossection is chosen because zero of such norms unambiguously indicates the decay of disturbances. The temporal evolution of these norms is shown in figure 7 for three sets of parameters. Even though the

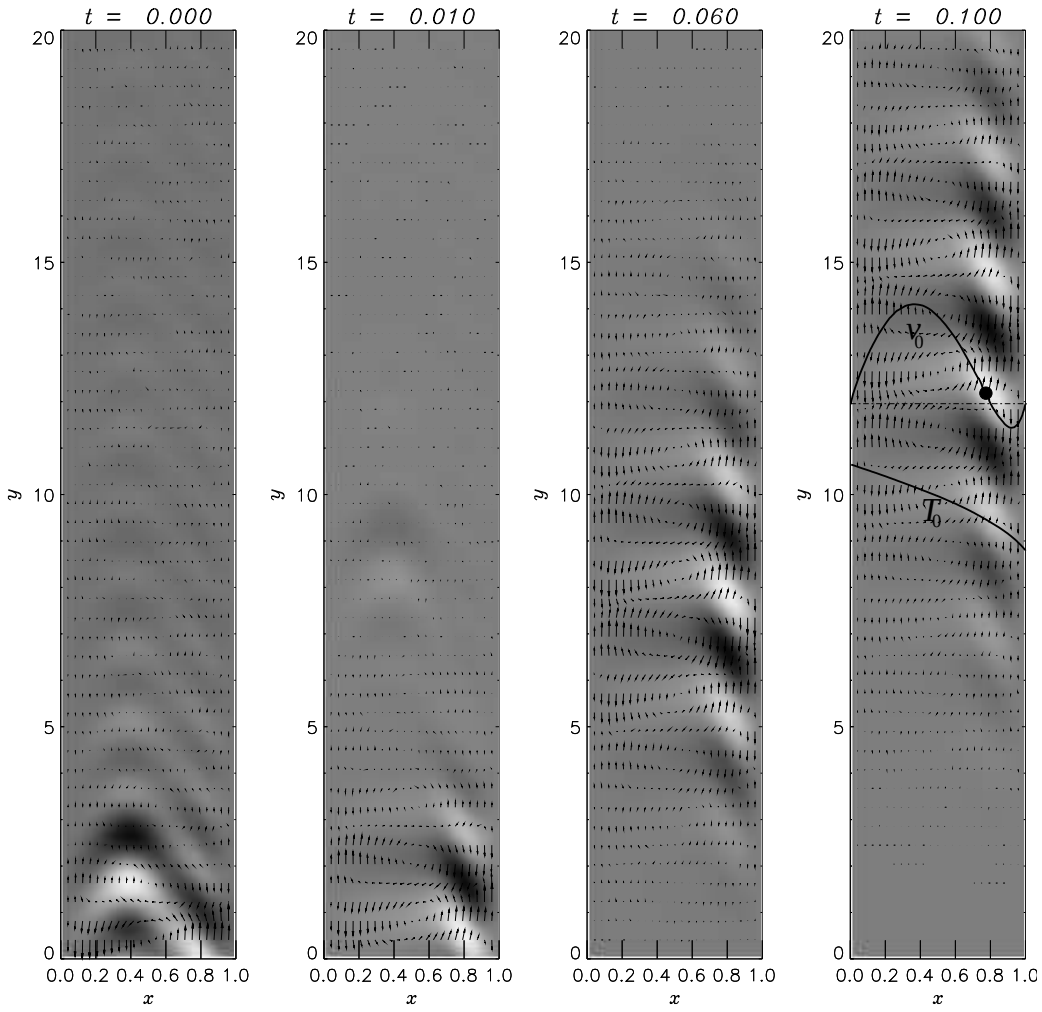

Fig. 6. Same as Fig. 3 but for $(Re, Gr, \epsilon) = (260, 46000, 0.6)$. Absolute instability. Shear mode.

curves obtained for the parameter set of figure 6 (dashed lines) indicate the norms decrease over the shown (transient) time interval they never decay to zero completely. This means that while the growing envelope of shear-driven disturbances moves away from its initial location as seen in figure 6 it leaves a non-decaying tail behind which is a characteristic feature of absolute instability. This cannot be seen in figure 6 directly because of the large difference between the disturbance amplitudes at $y = 0$ and at the centre of the propagating envelope: the relatively small amplitude disturbances near the origin cannot be graphically resolved within the used linear shade scale.

For comparison the time evolution of disturbance norms for two smaller values of the Grashof number are shown in figure 7 by the solid and dash-dotted lines. For both $Gr = 39000$ and $Gr = 42000$ the decay of disturbances at $y = 0$ is very quick while otherwise the instability patterns (not presented here) are

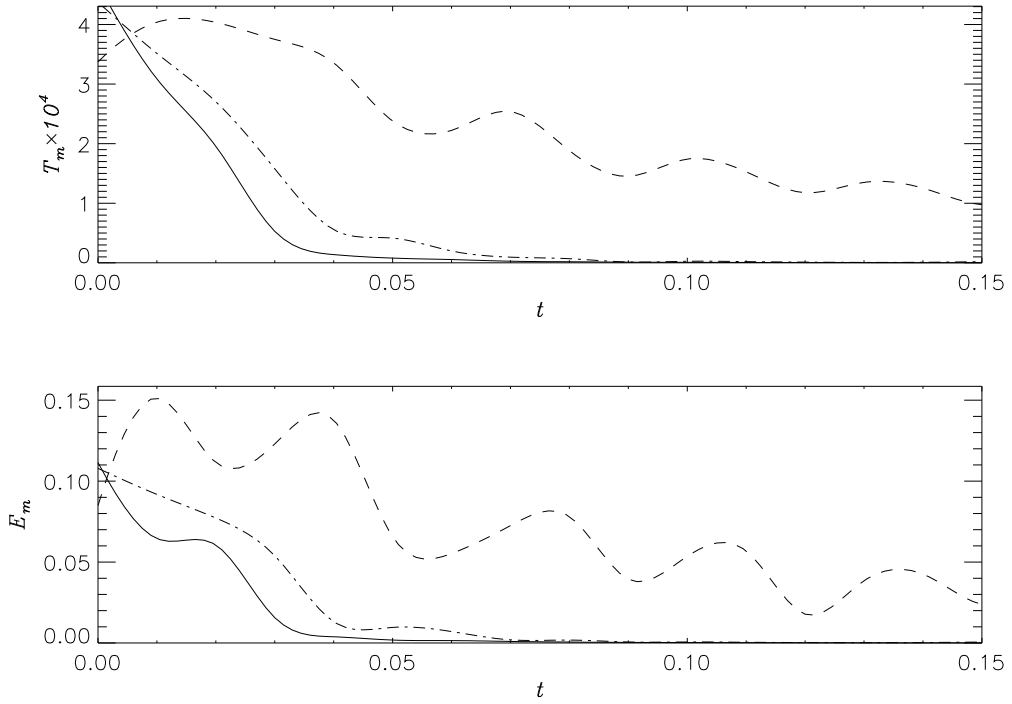

Fig. 7. Time history of norms T_m and E_m for the shear mode at $(Re, \epsilon) = (260, 0.6)$ and $Gr = 39000$ (solid lines, convective instability), $Gr = 42000$ (dash-dotted lines, convective instability) and $Gr = 46000$ (dashed lines, absolute instability).

very similar to those shown in figure 6. This is typical for convectively unstable systems. Indeed the analytical investigation reported in [1] demonstrated that both $Gr = 39000$ and $Gr = 42000$ regimes correspond to convective instability of non-Boussinesq shear-driven disturbances at $Re = 260$.

The dynamics of the buoyancy mode envelope is shown in figure 8 for the same set of governing parameters as in figure 6. It differs drastically from that of the shear mode. The buoyancy wave envelope propagates downwards i.e. in the direction opposite to that dictated by the applied pressure gradient. This is possible because buoyancy-driven instability arises near the cold wall i.e. in the region where basic flow is descending. As discussed earlier in this section the buoyancy-driven mode is characterised by a much longer wave length and a substantially smaller linear amplification rate σ^R. For this reason both the spatial scale and the observation time interval are much larger in figure 8 than those in figure 6. It can be seen from the rightmost plot in figure 8 that disturbances occupy the complete flow region even after a long observation time. This demonstrates the absolute character of the buoyancy-driven instability for $(Re, Gr, \epsilon) = (260, 46000, 0.6)$. The time history of norms (22) presented in figure 9 also confirms this conclusion.

The absolute character of a non-Boussinesq buoyancy-driven instability in

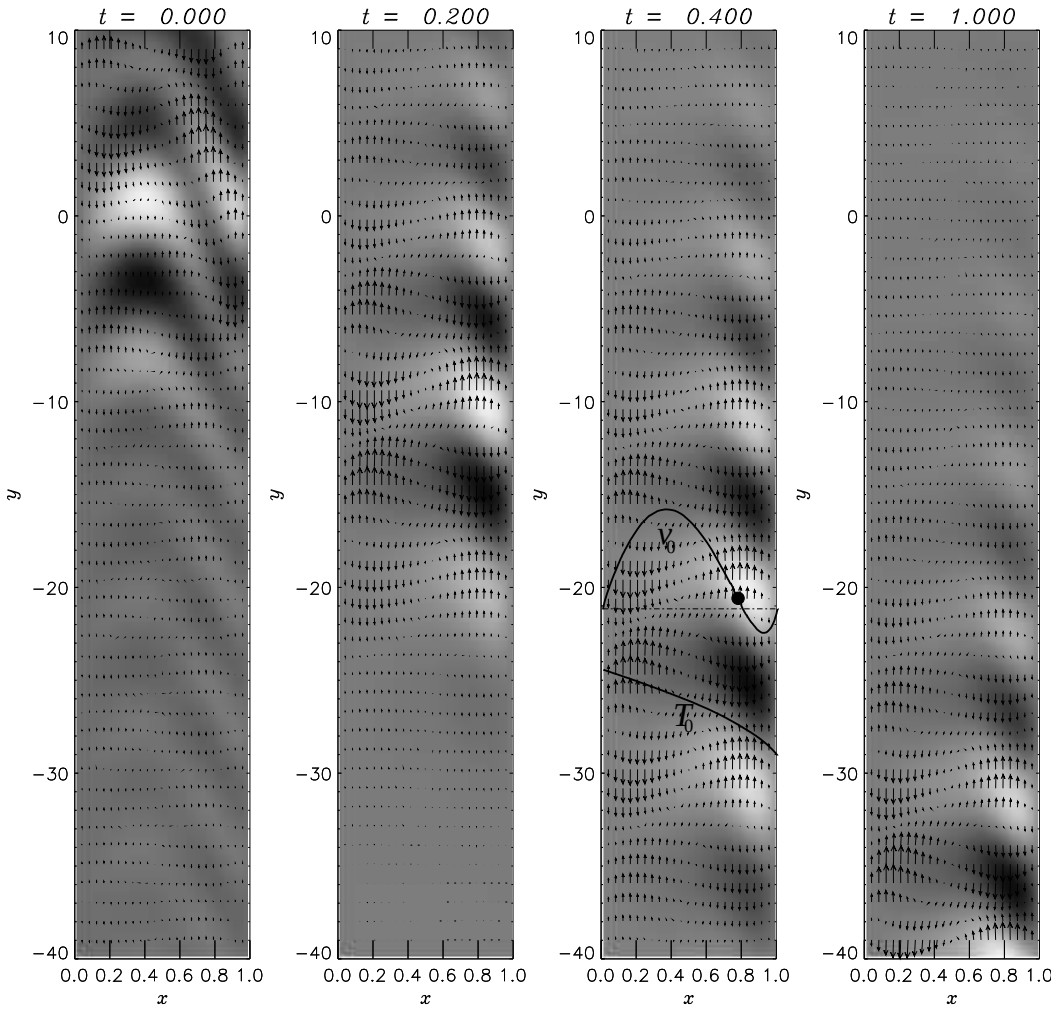

Fig. 8. Same as Fig. 3 but for $(Re, Gr, \epsilon) = (260, 46000, 0.6)$. Absolute instability. Buoyancy mode.

mixed-convection regimes (at $Re \neq 0$) is in contrast to the convective character found in the natural convection regime ($Re = 0$) depicted in figure 5. The transition between these two spatio-temporal instability scenarios is therefore due to the applied pressure gradient. While the buoyancy disturbances tend to propagate downwards the applied pressure gradient "pushes" these disturbance structures upwards. When the applied pressure gradient is sufficiently strong it sweeps the tail of a dropping buoyancy wave envelope upwards thus defining the transition to absolute instability. This conclusion is fully consistent with theoretical findings reported in [1] (specifically, see the discussions of zones $\mathbf{CAI}_1$ and $\mathbf{CAI}_2$ in figures 13 and 14 in [1]). It was found there that absolute instability of the buoyancy mode can only be observed when the pressure gradient forces the flow in the direction opposite to the gravity i.e. upwards.

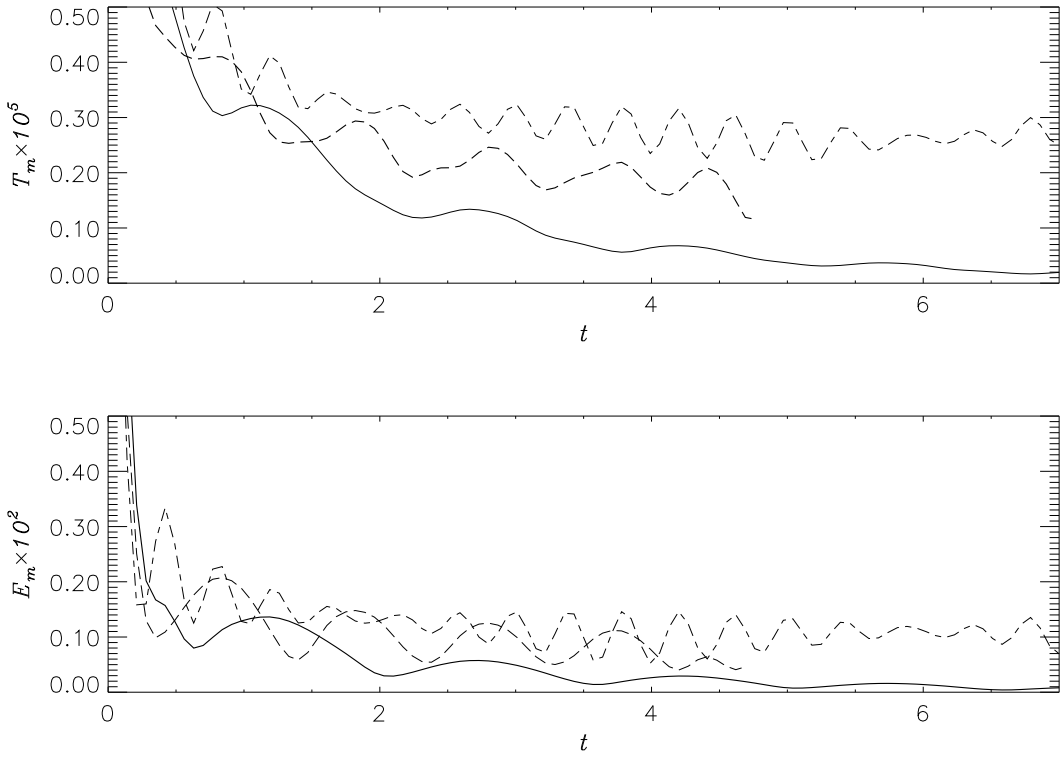

Fig. 9. Time history of norms T_m and E_m for the buoyancy mode at $(Re, \epsilon) = (260, 0.6)$ and $Gr = 39000$ (solid lines, convective instability), $Gr = 42000$ (dash-dotted lines, absolute instability) and $Gr = 46000$ (dashed lines, absolute instability).

For the fixed pressure gradient (Reynolds number) but reduced Grashof number, the buoyancy mode undergoes transition from absolute to convective instability, see solid lines in figure 9. The reasons for this transition are less obvious. Indeed there are two competing processes taking place when the Grashof number is reduced while the Reynolds number remains fixed. On the one hand, the basic flow velocity profile becomes more parabolic as the degree of the flow reversal due to the negative buoyancy near the cold wall decreases. Therefore the maximum downward basic flow velocity is decreased which creates better conditions for the the tail of the buoyancy wave envelope to move upwards as required for absolute instability. On the other hand the disturbance amplification rate σ^R, which is the major quantity related to the wave envelope extension rate [13], decreases with the decreasing Grashof number. The interplay between these two processes results in the observed transition from absolute to convective instability. This is also in agreement with [1].

The individual disturbance norms computed for $Re = 260$ and presented in figures 7 and 9 illustrate an intricate interplay between shear- and buoyancy-driven instabilities which results in a wealth of flow patterns in the considered non-Boussinesq mixed convection problem despite its very simple geometry. Indeed, for relatively low Grashof numbers ($Gr = 39000$) both shear and

buoyancy disturbances are convectively unstable and propagate in the opposite directions. Therefore it should be possible to detect these individual disturbance patterns experimentally or using direct numerical simulations of full equations. For intermediate values of the Grashof number ($Gr = 42000$) the buoyancy-driven instability becomes absolute while the shear-driven one remains convective. However the amplification rate of the buoyancy-driven disturbances is much smaller than that of the shear-driven ones, see figure 2(c). Therefore again it should be possible to observe both disturbances experimentally and numerically. It is expected that one would first observe a fast growing and moving upwards shear-driven envelope. However, once it propagates away, it will be replaced by a long-wave buoyancy-driven disturbance pattern eventually occupying the complete flow domain. In contrast, at larger values of the Grashof number ($Gr = 46000$) both instability modes are absolutely unstable and eventually should occupy the complete flow domain. However since the shear-driven mode has a much larger amplification rate it is unlikely that experimental observation or direct numerical simulations will be capable of clearly distinguishing between these two instabilities. It is possible though that some analytical progress can be made for such regimes using weakly non-linear reduction as was outlined in [29].

As a side remark, note that in figure 9 the dashed lines representing a quickly developing absolute buoyancy-driven instability at $Gr = 46000$ are truncated at $t \approx 4.7$. This is because, as discussed in Section 3.1, the low level noise in the initial conditions distributed throughout the computational domain is amplified exponentially. It obscures the evolution of the localised structure of interest for large times. Due to such exponential noise amplification the accurate direct numerical evaluation of integral (21) for a fixed spatial location can only be performed for a limited time no matter how accurate the chosen integration scheme is. This conclusion is in accord with the discussion given in [26].

4 Conclusions

By evaluating directly the Fourier integrals representing linearised disturbances arising from an initially localised source the theoretical conclusions made in the previous work [1] on the spatio-temporal nature of instabilities appearing in mixed convection flows of air between vertical differentially heated planes have been re-affirmed and extended. The flow patterns computed for a number of representative regimes confirm that in the Boussinesq limit of small temperature differences between the channel walls the natural convection is absolutely unstable and forced convection is convectively unstable when the Grashof and Reynolds numbers are sufficiently large and a linear instability is triggered. The physical nature of instabilities found in the Boussinesq limit is

the shear of the flow. The conducted investigation revealed that in contrast to Boussinesq flows the instabilities in high-temperature non-Boussinesq convection can be triggered by two distinct physical mechanisms: shear and buoyancy. The interplay between these two modes defines a remarkable variety of the spatio-temporal instability patterns. The most interesting of them, convectively unstable natural convection due to the buoyancy mode and multi-mode convective/convective, convective/absolute and absolute/absolute instabilities due to the combined action of the shear and buoyancy modes are presented and contrasted with their Boussinesq counterparts. The current computations are in full agreement with the previously published semi-analytical results of [1] and provide a physical insight into instability phenomena which would be hard or impossible to obtain using DNS or experimental observations.

We have also discussed the limitations and shortcomings of the numerical integration technique which are of a generic nature and are relevant to applications beyond the physical scope of the present investigation. It is shown that special care should be taken in interpreting spatio-temporal patterns computed by direct numerical evaluation of the Fourier integrals in order to obtain a true description of the character of instabilities especially when they develop on substantially different time scales.

This work was partially supported by a computing grant from the Australian Partnership for Advanced Computing.

References

[1] S. A. Suslov, Spatio-temporal instabilities in non-Boussinesq convection, Teor. Comp. Fluid Dyn. 21 (4) (2007) 271–290.

[2] G. Batchelor, Heat transfer by free convection across a closed cavity between vertical boundaries at different temperatures, Quart. Appl. Math. XII (1954) 209–233.

[3] E. Eckert, W. Carlson, Natural convection in an air layer enclosed between two vertical plates with different temperatures, Int. J. Heat Mass Transfer 2 (1961) 106–120.

[4] R. N. Rudakov, Spectrum of perturbations and stability of convective motion between vertical plates, Appl. Math. Mech. 31 (1967) 376–383.

[5] K. Fukui, M. Nakajima, H. Ueda, K. Suzaki, T. Mizushina, Flow instability and transport phenomena in combined free and forced convection between vertical parallel plates, J. Chem. Eng. Japan 15 (1982) 172–180.

[6] Y. Lee, S. A. Korpela, Multicellular natural convection in a vertical slot, J. Fluid Mech. 126 (1983) 91–121.

[7] S. Wakitani, Flow patterns of natural convection in an air-filled vertical cavity, Phys. Fluids 10 (8) (1998) 1924–1928.

[8] R. F. Bergholtz, Instability of steady natural convection in a vertical fluid layer, J. Fluid Mech. 84 (1978) 743–768.

[9] J. Mizushima, K. Gotoh, Nonlinear evolution of the disturbance in a natural convection induced in a vertical fluid layer, J. Phys. Soc. Japan 52 (1983) 1206–1214.

[10] S. A. Suslov, S. Paolucci, Stability of natural convection flow in a tall vertical enclosure under non-Boussinesq conditions, Int. J. Heat Mass Transfer 38 (1995) 2143–2157.

[11] S. A. Suslov, S. Paolucci, Stability of mixed-convection flow in a tall vertical channel under non-Boussinesq conditions, J. Fluid Mech. 302 (1995) 91–115.

[12] S. A. Suslov, S. Paolucci, Nonlinear stability of mixed convection flow under non-Boussinesq conditions. Part 1. Analysis and bifurcations, J. Fluid Mech. 398 (1999) 61–85.

[13] S. A. Suslov, S. Paolucci, Stability of non-Boussinesq convection via the complex Ginzburg-Landau model, Fluid Dyn. Res. 35 (2004) 159–203.

[14] B. Zamora, J. Hernández, Influence of variable property effects on natural convection flows in an asymmetrically-heated vertical channels, Int. Comm. Heat Mass Transfer 24 (8) (1997) 1153–1162.

[15] J. Zhang, S. Childress, A. Libchaber, Non-Boussinesq effect: Thermal convection with broken symmetry, Phys. Fluids 9 (4) (1997) 1034–1042.

[16] J. Zhang, S. Childress, A. Libchaber, Non-Boussinesq effect: Asymmetric velocity profiles in thermal convection, Phys. Fluids 10 (8) (1998) 1534–1536.

[17] J. Wright, H. Jin, K. Hollands, D. Naylor, Flow visualisation of natural convection in a tall air-filled vertical cavity, Int. J. Heat and Mass Transfer 49 (2006) 889–904.

[18] S. Paolucci, On the filtering of sound from the Navier-Stokes equations, Tech. Rep. SAND82-8257, Sandia National Laboratories, Livermore, California (1982).

[19] D. R. Chenoweth, S. Paolucci, Gas flow in vertical slots with large horizontal temperature differences, Phys. Fluids 28 (1985) 2365–2374.

[20] D. R. Chenoweth, S. Paolucci, Natural convection in an enclosed vertical air layer with large horizontal temperature differences, J. Fluid Mech. 169 (1986) 173–210.

[21] S. A. Suslov, S. Paolucci, Nonlinear stability of mixed convection flow under non-Boussinesq conditions. Part 2. Mean flow characteristics, J. Fluid Mech. 398 (1999) 87–108.

[22] R. J. Deissler, The convective nature of instability in plane Poiseuille flow, Phys. Fluids 30 (1987) 2303–2305.

[23] D. Hatziavramidis, H.-C. Ku, An integral Chebyshev expansion method for boundary-value problems of O.D.E. type, Comp. & Maths with Appls 11 (6) (1985) 581–586.

[24] F. M. White, Viscous Fluid Flow, McGraw-Hill, 1974.

[25] H.-C. Ku, D. Hatziavramidis, Chebyshev expansion methods for the solution of the extended Graetz problem, J. Comput. Phys. 56 (1984) 495–512.

[26] P. Carrière, P. A. Monkewitz, Convective versus absolute instability in mixed Rayleigh-Bénard-Poiseuille convection, J. Fluid Mech. 384 (1999) 243–262.

[27] G. F. Spooner, W. O. Criminale, The evolution of disturbances in an Ekman boundary layer, J. Fluid Mech. 115 (1982) 327.

[28] P. G. Drazin, W. H. Reid, Hydrodynamic Stability, 2nd Edition, Cambridge University Press, 2004.

[29] S. Suslov, Multi-mode spatiotemporal instability in non-Boussinesq convection, ANZIAM Journal (electronic), http://anziamj.austms.org.au/V45/CTAC2003, 45(E) (2004) C149–C162.